*Int. J. Electrochem. Sci.*, 14 **(2019)** 3856 – 3870, doi: 10.20964/2019.03.01

International Journal of
ELECTROCHEMICAL
SCIENCE
www.electrochemsci.org

# Activated Porous Carbon Nanofibers for High-Performance Supercapacitors

*Moyinul Islam, Xing Lu* *

State Key Laboratory of Materials Processing and Die & Mold Technology, School of Materials Science and Engineering, Huazhong University of Science and Technology, Wuhan 430074, P. R. China
*E-mail: lux@hust.edu.cn

*Received:* 23 November 2018 / *Accepted:* 27 December 2018 / *Published:* 10 March 2019

The pursuit of high-capacitance carbon materials is urgently needed for supercapacitors, which are among the most promising energy storage devices. Herein, we developed an effective KOH-activation method to improve the porous structures of electrospun carbon nanofibers for high-performance supercapacitors. In detail, polyacrylonitrile (PAN) and polymethyl methacrylate (PMMA) polymer blend solutions were electrospun to fabricate carbon nanofibers for pure PAN and, PAN:PMMA (80:20). PMMA was used as a sacrificial polymer to create pores. Furthermore, the KOH-activation method was applied to improve the pores of PAN:PMMA (80:20) at 600º C. The obtained KOH-activated PAN:PMMA (80:20) exhibits an excellent specific capacitance of 440 F $g^{-1}$ at a current density of 0.25 A $g^{-1}$ and a superior cycling stability of 95% after 5000 cycles. The present research contributes to the implementation of KOH-activation that results in excellent performance compared to carbon nanofibers reported thus far. Our work demonstrates that KOH-activation is an outstanding method to promote the performance of supercapacitors. Therefore, such a strategy could be a promising method to fabricate high-performance supercapacitors.

**Keywords:** Activation, Carbon nanofibers, Supercapacitors

## 1. INTRODUCTION

Supercapacitors are promising electrical energy storage devices with a high power density, fast charge-discharge rate and long cycle lifetime [1-5]. Carbon-based materials such as activated carbon, graphene, carbon nanotubes, and carbon nanofibers play a central role in supercapacitors [6-12]. Among them, carbon nanofibers are promising electrode materials because of their outstanding properties, such as high stability and nanostructured networks for efficient electron transport,[13] high conductivity, excellent mechanical strength, and controllable pore size [14]. Carbon nanofibers represent an ideal

material for application in electric double layer capacitors. They generally exhibit an open, mesoporous structure and good conductivity [15]. Carbon nanofibers have diameters between 50 and 500 nm with an average pore size of 3–20 nm, and activation can lead to the opening of smaller pores. Due to the morphology of activated carbon nanofibers, most of the porosity is situated on the surface of the fibers, leading to easily accessible active sites [14, 16, 17].

Electrospinning is a simple and widely used technique to produce nanofibers with controlled diameter, fiber alignment, and uniform shape [18-23]. The PAN and PMMA immiscible polymer solution is an easy route to obtain carbon materials with fine and controlled pores [24, 25]. PAN was chosen as the carbon precursor due to its good thermal stability, excellent spin ability, and commercial availability [26-31]. The pore size of nanofibers can be controlled by varying the amount of PMMA in the blend compositions [32, 33].

Meanwhile, KOH-activation has attracted immense attention because it is an easy process to improve the pore size [34-36]. In general, KOH can generate micropores and mesopores in various carbon frameworks [37]. Several studies have reported the activation of nanofibers for high-performance supercapacitors [29, 32, 38, 39]. Geon and co-authors reported the fabrication of carbon nanofibers using Nafion as a sacrificial polymer, and $HNO_3$ was used for activation. The prepared nanofibers exhibited a specific capacitance of 207 F $g^{-1}$ at a current density of 0.2 A $g^{-1}$ and capacitance retention of 93% after 3000 cycles [39]. Daniel and co-authors investigated high-energy density nanofibers using polyvinylpyrrolidone (PVP) followed by KOH-activation. The authors obtained a specific capacitance of 144 F $g^{-1}$ and specific energy of 61 W h $kg^{-1}$ respectively [38]. However, the specific capacitance and cycling stability are still needed to improve for high-performance supercapacitors.

In this study, we developed an effective KOH-activation method to improve the porous structure of electrospun carbon nanofibers and their capacitive performance. Our work demonstrates that KOH-activation is an outstanding method for fabricating porous carbon nanofibers with excellent capacitive performance (440 F $g^{-1}$ at a current density of 0.25 A $g^{-1}$) and superior cycling stability (95%). To the best of our knowledge, this is the first study on KOH-activation with PAN and PMMA as supercapacitor electrode materials. We believe that such a KOH-activated material might become a promising candidate for high-performance supercapacitors.

## 2. EXPERIMENTAL

### *2.1 Materials*

Polyacrylonitrile (PAN, Mw = 150 000 g $mol^{-1}$) was purchased from Sigma-Aldrich. Polymethyl methacrylate (PMMA, Mw = 120 000 g $mol^{-1}$) and N, N-dimethylformamide (DMF) were purchased from Sinopharm Chemical Reagent Co, Ltd. and used as received.

### *2.2 Fabrication of carbon nanofibers by electrospinning*

Pure PAN and PAN:PMMA (80:20) immiscible polymer blends were dissolved in 10 mL DMF in separate vials overnight at 80º C. The solutions were electrospun under an applied voltage of 18 kV

(Gamma High Voltage Research, Inc., power supply). The polymer solutions were loaded into a syringe, and the attached needle tip was connected to the positive voltage of the power supply. The volume of the polymer solutions was 5 mL $h^{-1}$ which was delivered to the tip at a constant flow rate of 0.8 mL $h^{-1}$ controlled by a syringe pump and the aluminum foil was placed 15 cm away from the needle tip as a collector. The resultant nanofiber mats were separated from the aluminum foil and cut into small sections for heat treatment in a tube furnace, wherein the samples were first stabilized at 280 ºC for 2 h under the air flow at a heating rate of 2 ºC $min^{-1}$. The stabilized mats were further annealed in a tube furnace under $N_2$ flow at 800 ºC for 2 h at a heating rate of 5 ºC $min^{-1}$. The heat treatments converted PAN to carbon fibers and decomposed the PMMA to form porous carbon nanofibers. PAN:PMMA (95:05), PAN:PMMA (90:10), and PAN:PMMA (60:40) were also prepared using the same procedure.

### *2.3 KOH-activation of porous carbon nanofibers*

Porous carbon nanofibers were immersed in a KOH:deionized water (30:70) solution overnight. Then, the thermal treatment was performed in flowing nitrogen in a tube furnace at 600 ºC for 30 min at a heating rate of 5 ºC $min^{-1}$. After that, the activated samples were washed sequentially with diluted 0.1 M HCl solution and distilled water until the $p^H$ of the filtrates became neutral. Finally, the samples were dried in an oven at 60 ºC overnight to obtain the final solid sample of KOH-activated PAN: PMMA (80:20).

### *2.4 Materials characterization*

The morphology of the obtained carbon nanofibers was analyzed by scanning electron microscopy, SEM (NOVA Nano SEM 450) and high-resolution transmission electron microscopy, HR-TEM (FEI Tecnai G2 F30). The Brunauer-Emmett-Teller (BET) surface area and the pore size of the fibers were evaluated from $N_2$ adsorption-desorption isotherms recorded at 300 K using an autosorb-1C machine (Quanta chrome, USA). The X-ray diffraction (XRD) patterns were recorded on a Shimadzu XRD-700 X-ray diffractometer with Cu Kα radiation (λ =0.1541 nm, operated at 40 kV and 40 mA). Cyclic voltammetry (CV), galvanostatic charge-discharge (GCD) and electrochemical impedance spectroscopy (EIS) were measured by a CHI 660E electrochemical workstation. The working electrode was prepared as follows: the working material was mixed with acetylene black as a conductive agent and polytetrafluoroethylene (PTFE) as a binder in a weight ratio of 80:10:10. DMF was used as the solvent. For a typical three-electrode system, platinum (Pt.) foil and Ag/AgCl were used as the counter electrode and reference electrode, respectively. All the supercapacitor tests were performed using 6 M KOH aqueous solution as an electrolyte.

## 3. RESULTS AND DISCUSSION

Carbon nanofibers were fabricated by electrospinning PAN as the precursor and 20% PMMA as the sacrificial polymer to obtain the porous structure [32]. The mesoporous carbon nanofiber electrode

materials are obtained by KOH-activation (Scheme. 1). The pore size can be controlled by varying the amount of PMMA in the blend compositions. There are no pores in the PAN:PMMA (95:05) and, very few small pores in the PAN:PMMA (90:10). The porous structures are broken in the PAN:PMMA (60:40) due to the excess loading of PMMA, while many pores are present in PAN:PMMA (80:20) with a slightly rough surface. We found PAN:PMMA (80:20) to be the optimum blend composition among those samples (Fig. S1-S4).

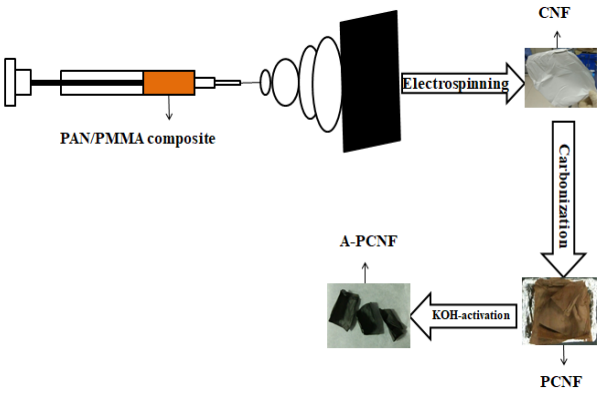


**Scheme 1.** Schematic illustration for the fabrication of A-PCNF.

The carbonized pure PAN, PAN:PMMA (80:20), and KOH-activated PAN:PMMA (80:20) were designated as carbon nanofiber (CNF), porous carbon nanofiber (PCNF), and KOH-activated porous carbon nanofiber (A-PCNF), respectively. The morphologies of the CNF, PCNF, and A-PCNF were characterized by SEM. CNF shows a fiber-like morphology with an average diameter of approximately 500–550 nm and a plane surface (Fig. 1a and Fig. S5). A-PCNF shows a smooth surface with large pores owing to KOH-activation, whereas PCNF shows a rough surface (Fig. 1b and Fig. 1c). In the case of PCNF, the discontinuous PMMA phase in the polymeric blend burns out during carbonization [24], and the morphology of A-PCNF is well maintained and fiber-like even after activation at 600 ºC compared to PCNF (Fig. S6 and Fig. S7).

HR-TEM measurements were performed to further investigate the morphological and structural properties of CNF, PCNF, and A-PCNF. CNF shows a very smooth and uniform shape (Fig. 2a), while PCNF and A-PCNF show a porous structure because the PMMA phase decomposes to produce a pore creating material via thermal decomposition and the PAN phase is easily transformed into carbon during heat treatment at 800 ºC (Fig. 2b and Fig. 2c) [40].

To investigate the pore structures and surface properties, nitrogen adsorption-desorption isotherms were obtained by BET measurements (Fig. 3a). The isotherms of CNF, PCNF, and A-PCNF show Type IV characteristics that indicate the existence of mesopore structures (2–50 nm). Nitrogen adsorption in the low-pressure region is associated with the filling of micropores, whereas adsorption in the high-pressure region is due to the mesopores that are created mainly due to the burning out of the PMMA during thermal treatment [33]. Fig. 3b presents the BJH analysis for the pore size distribution and pore volume in the mesopore size range of 2.6–20 nm. A-PCNF shows the highest mesopore volume at approximately 4 nm.

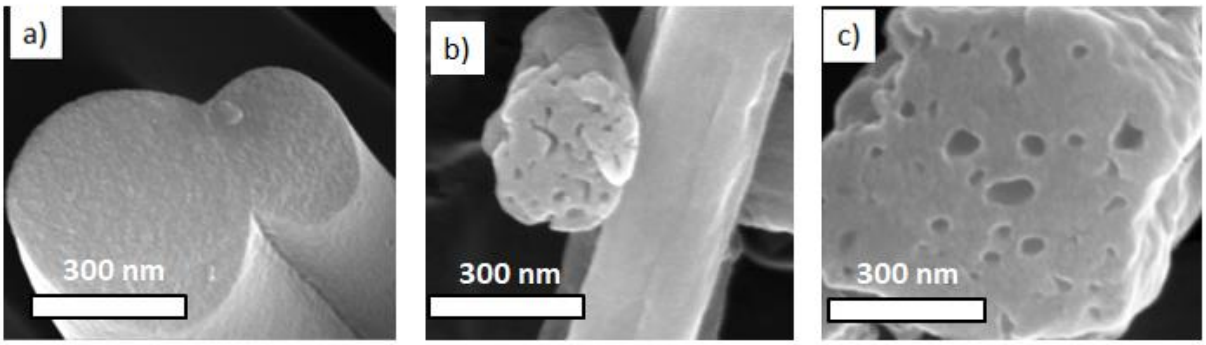


**Figure 1.** SEM images of the surface morphology of (a) CNF, (b) PCNF, and (c) A-PCNF.

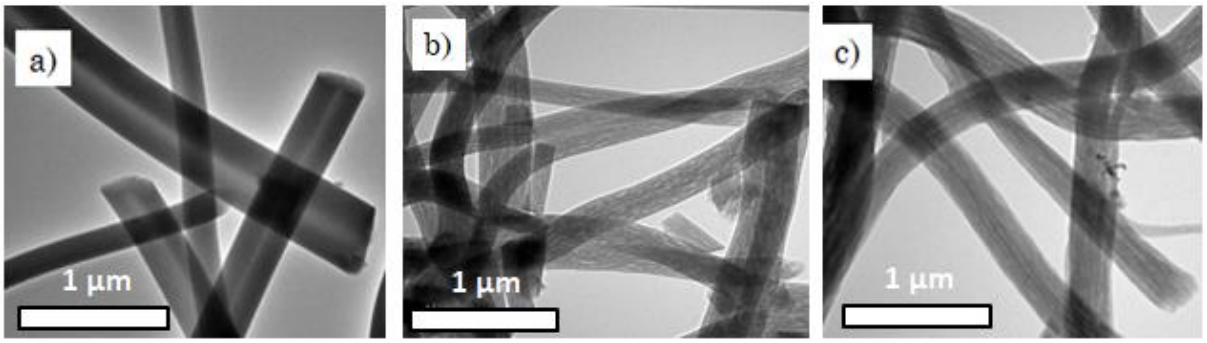


**Figure 2.** HR-TEM images of (a) CNF, (b) PCNF, and (c) A-PCNF.

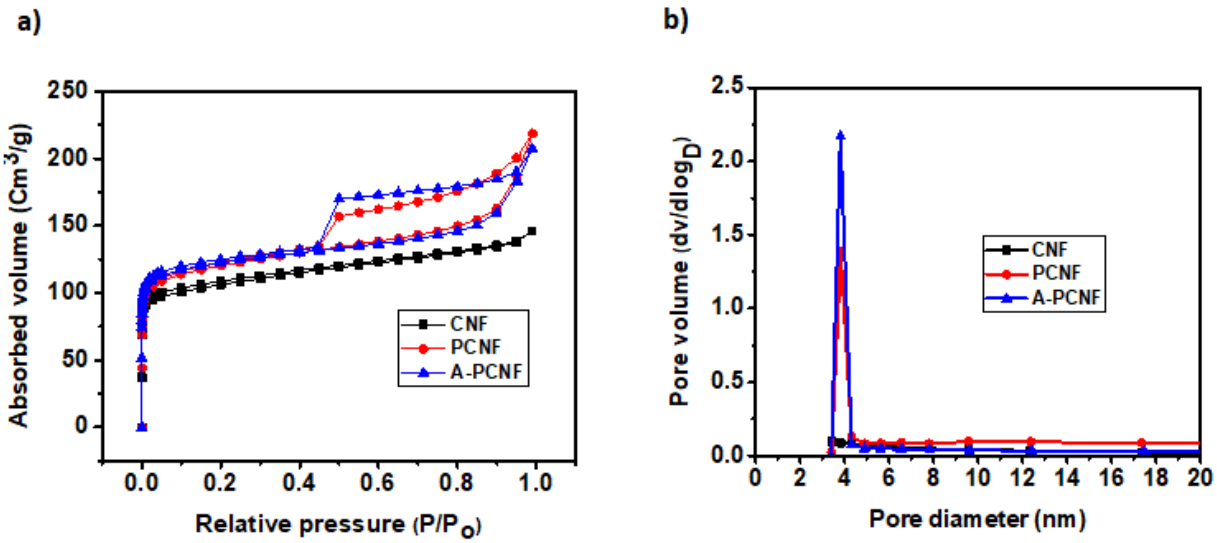


**Figure 3.** (a) $N_2$ adsorption-desorption isotherms of CNF, PCNF, and A-PCNF. (b) BJH pore size distributions of CNF, PCNF, and A-PCNF.

Detailed results of the BET measurements, including specific surface area, total pore volume, and average pore diameter of CNF, PCNF, and A-PCNF are summarized in Table 1. The pore size distribution and mesopores volume are known to be important aspects for high-performance

supercapacitors at high current density [39]. The crystalline structures of CNF, PCNF, and A-PCNF were characterized by XRD analysis (Fig. S8). Broad diffraction peaks corresponding to the (002) layers of graphite are observed at approximately 2θ = 25º [41, 42]. The XRD patterns suggest that all samples are amorphous carbon materials.

**Table 1.** List of the specific surface area, total pore volume and average pore diameter of the CNF, PCNF, and A-PCNF.

| Samples | $S_{BET}$ ($m^2 g^{-1}$) | Total pore volume ($cm^3 g^{-1}$) | Average diameter (nm) |
|---|---|---|---|
| CNF | 404 | 0.22 | 2.24 |
| PCNF | 654 | 0.32 | 2.72 |
| A-PCNF | 871 | 0.38 | 2.98 |

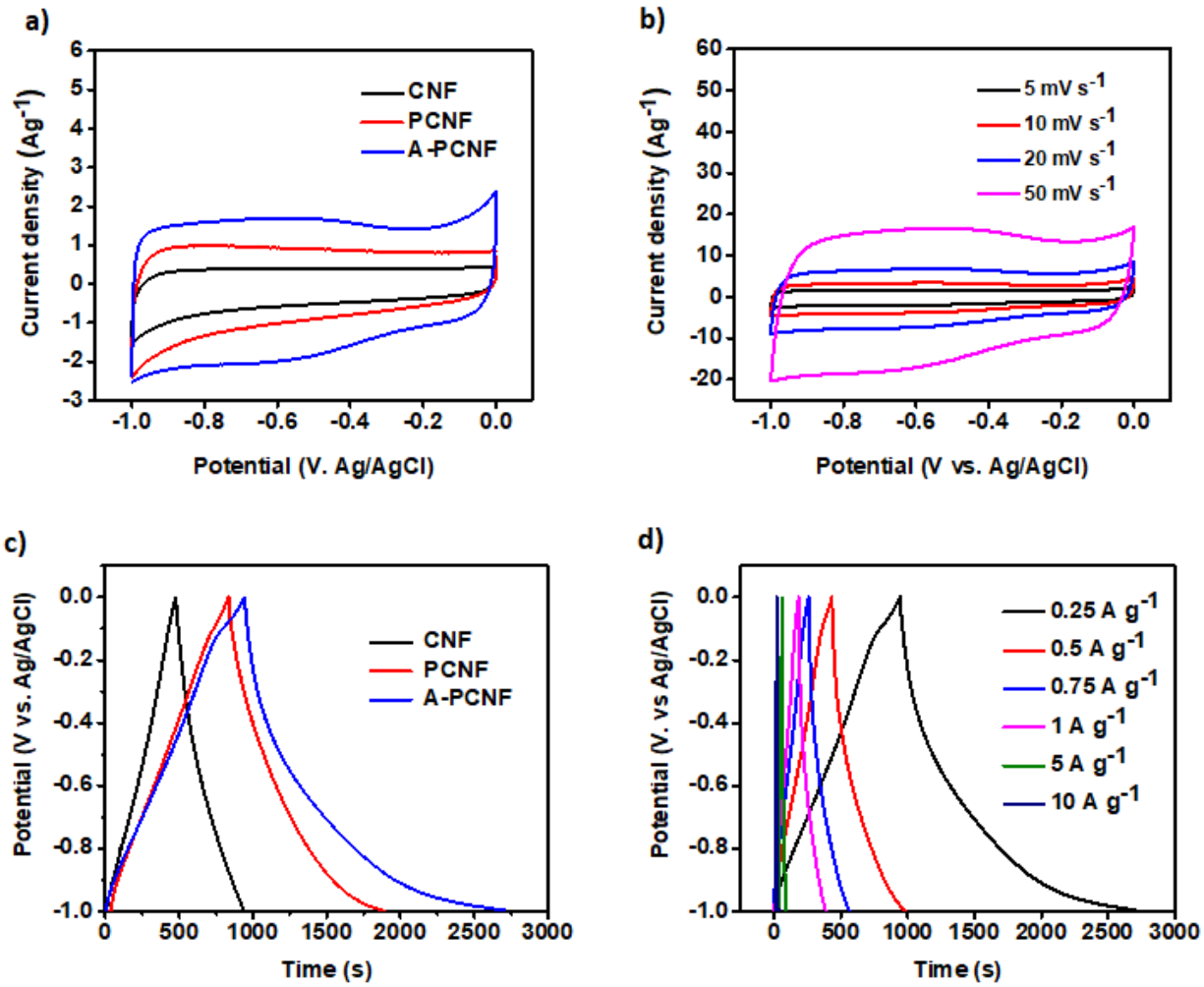


**Figure 4.** (a) CV curves of CNF, PCNF, and A-PCNF at scan rate of 5 mV $S^{-1}$. (b) CV curves of A-PCNF at scan rates of 5 mV $S^{-1}$, 10 mV $S^{-1}$, 20 mV $S^{-1}$ and 50 mV $S^{-1}$. (c) GCD curves of CNF, PCNF, and A-PCNF at a current density of 0.25 A $g^{-1}$. (d) GCD curves of A-PCNF at different current density ranging from 0.25 to 10 A $g^{-1}$.

The electrochemical capacitive performance of CNF, PCNF, and A-PCNF was evaluated with a three-electrode system in 6.0 M aqueous KOH solution under the voltage range from –1 to 0 V (vs. Ag/AgCl). A-PCNF shows a quasi-rectangular shape at a scan rate of 5 mV $s^{-1}$ (Fig. 4a), which can be attributed to the excellent electric double layer capacitive behavior. The A-PCNF was further investigated by CV testing at various scan rates ranging from 5 to 50 mV $s^{-1}$ (Fig. 4b). Nearly rectangular CV curves for A-PCNF, even at a scan rate of 50 mV $s^{-1}$, reveal good electrochemical supercapacitive performance.

GCD measurements were performed to further investigate the electrochemical performances of CNF, PCNF, and A-PCNF. The specific capacitances of the CNF, PCNF, and A-PCNF electrodes were calculated to be 116, 261, and 440 F $g^{-1}$ at a current density of 0.25 A $g^{-1}$ (Fig. 4c). It is clear that the electrochemical capacitances of A-PCNF were remarkably enhanced after KOH-activation. The approximately linear lines with near triangular shapes are shown in Fig. 4d. The capacitance of A-PCNF decreases as the current density increases from 0.25 A $g^{-1}$ to 10 A $g^{-1}$. It is obvious that the capacitance of A-PCNF is still retained at 100 F $g^{-1}$ even at a current density of 10 A $g^{-1}$ (Fig. S9). These results may demonstrate that the A-PCNF electrode continued to deliver specific capacitance by efficient ion diffusion and continuous electron pathways [40]. The gravimetric capacitances of CNF, PCNF, and A-PCNF also decrease gradually as the ions in the electrolyte cannot fully access the surfaces of the fibers at a current density of 1 A $g^{-1}$ (Fig. S10) [43]. Notably, the performance of A-PCNF improved dramatically after KOH-activation, which is a better result than for CNF.

**Table 2.** Comparison of electrochemical performances for CNFs electrode materials.

| CNFs-based electrodes | Specific capacitance (F $g^{-1}$) | Capacitance retention (%) | Cycle number | Electrolyte | Reference |
|---|---|---|---|---|---|
| CNFs | 98 (0.5 A $g^{-1}$) | 96 | 300 | 1 M $H_2SO_4$ | [43] |
| BO-CNFs film | 192 (1 A $g^{-1}$) | 87 | 500 | 1 M $H_2SO_4$ | [44] |
| Porous CNFs | 104.5 (0.2 A $g^{-1}$) | 94 | 200 | 0.5M $H_2SO_4$ | [45] |
| Cross-linked N-doped CNFs | 175 (50 A $g^{-1}$) | 78.5 | 200 | 1 M $H_2SO_4$ | [15] |
| Activated CNFs | 93 (0.2 A $g^{-1}$) | 93 | 300 | 6 M KOH | [39] |
| Hollow CNFs | 105 (2 A $g^{-1}$) | 80 | 300 | 6 M KOH | [33] |
| Hybrid CNFs | 360 (0.3 A $g^{-1}$) | 90 | 200 | 3 M KOH | [46] |
| $MnO_2$-deposited CNFs | 67 (1 A $g^{-1}$) | 98.95 | 100 | 1M $Na_2SO_4$ | [47] |
| $N_2$-doped CNFs | 188 (0.5 A $g^{-1}$) | 97.5 | 500 | 6 M KOH | [48] |
| KOH-activated porous CNFs | 440 (0.25 A $g^{-1}$) | 95 | 500 | 6 M KOH | This work. |

Table 2 summarizes the electrochemical performances of several reported CNFs electrode materials in aqueous electrolytes for high-performance supercapacitors. It is obvious that the A-PCNF shows a superior specific capacitance of 440 F $g^{-1}$ while maintaining excellent cycling stability (95% after 5000 cycles). Therefore, such a KOH-activation method could be an outstanding strategy to fabricate carbon nanofiber materials for high-performance supercapacitors [46-48].

ElS measurements were used to obtain information on the performance of the supercapacitors. The Nyquist plots of CNF, PCNF, and A-PCNF are characterized by a semicircle in the high-frequency region and a vertical curve in the lower frequency region (Fig. 5a). A-PCNF and PCNF exhibit low charge transfer resistance ($R_{ct}$), and thus high conductivity. In contrast, CNF shows a relatively large semicircle and a large charge transfer resistance. The semicircles at the high-frequency region and vertical slopes at the lower frequency region (inset Fig. 5a) show the ion transport electrode/electrolyte interface, which is referred to as charge transfer capacitive behavior. Additionally, the intersection of a curve at the real resistance ($Z'$) axis is relative to the internal or equivalent series resistance (ESR) [49].

The cycling stability of supercapacitors is a crucial factor for their practical application. Excellent cycling stability of the A-PCNF was obtained by the GCD test at a current density of 1 A $g^{-1}$ (Fig. 5b). The results reveal that approximately 95% of the specific capacitance of A-PCNF is retained after 5000 charging-discharging cycles. Therefore, A-PCNF could facilitate electrolyte ion diffusion and electron transport, leading to reduced internal resistance and improved electrochemical capacitive performance for supercapacitors [45].

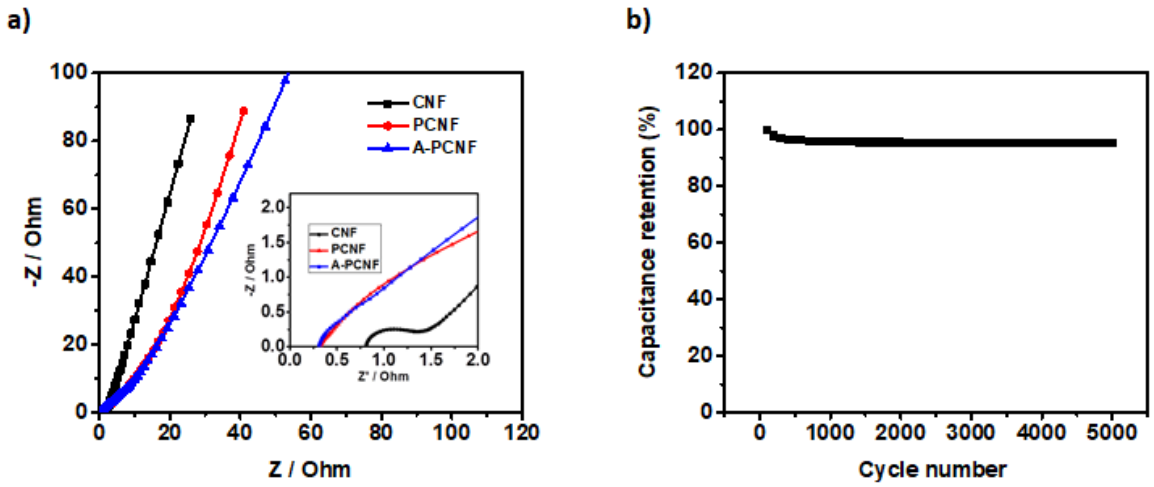


**Figure 5.** (a) Nyquist plots of CNF, PCNF, and A-PCNF. (b) Cycling performance of A-PCNF at a current density of 1 A $g^{-1}$.

## 4. CONCLUSIONS

We improved a KOH-activation method and synthesized mesoporous carbon nanofiber electrode materials by PAN and PMMA immiscible polymer solutions for high-performance supercapacitors. The obtained A-PCNF shows superior electrochemical capacitive properties, such as specific capacitance (440 F $g^{-1}$ at a current density of 0.25 A $g^{-1}$) and excellent cycling stability of 95% that was retained after 5000 cycles. This performance is much better than that of conventional electrospun carbon nanofibers

reported in the past few decades. Our results demonstrate that A-PCNF is a promising electrode material to improve the performance of supercapacitors. Therefore, such a KOH-activation method could be an outstanding strategy to fabricate porous carbon nanofiber materials for high-performance supercapacitors.

ACKNOWLEDGEMENTS
This work was financially supported by The National Natural Science Foundation of China (Nos. 51472095, 51672093, 51602112, and 51602097). The authors thank the Analytical and Testing Center in Huazhong University of Science and Technology for related measurements and instrumentation supports.

SUPPLEMENTARY MATERIALS

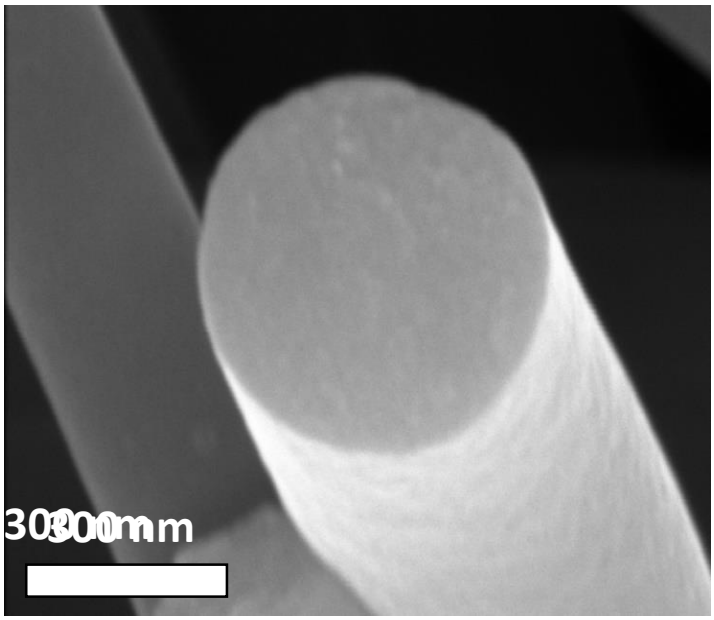


**Fig. S1.** SEM image of PAN:PMMA (95:05).

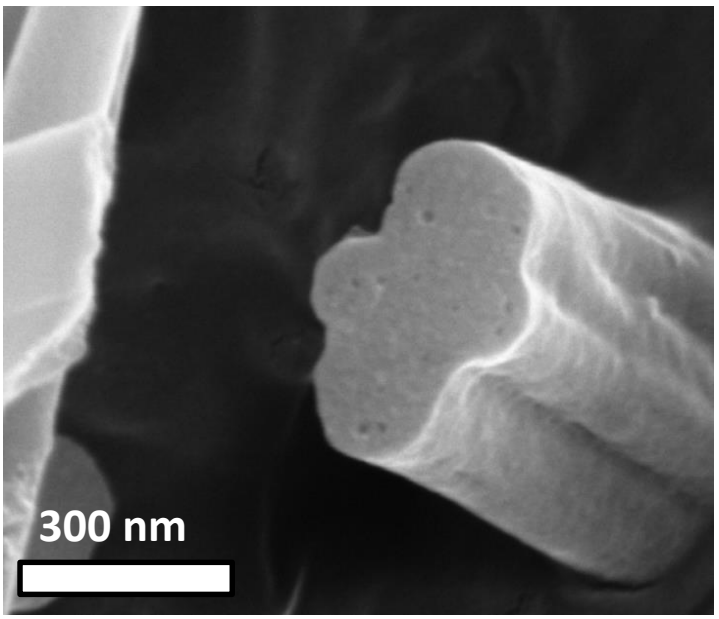


**Fig. S2.** SEM image of PAN:PMMA (90:10).

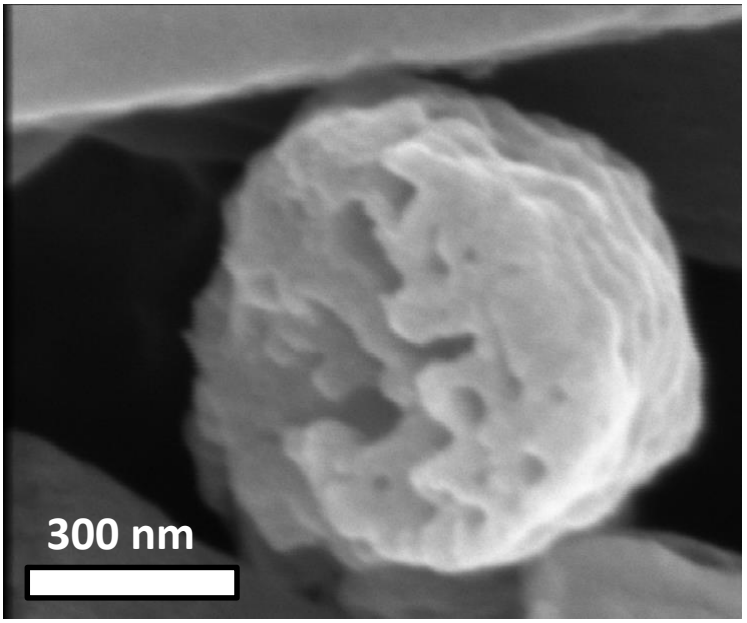


**Fig. S3.** SEM image of PAN:PMMA (60:40).

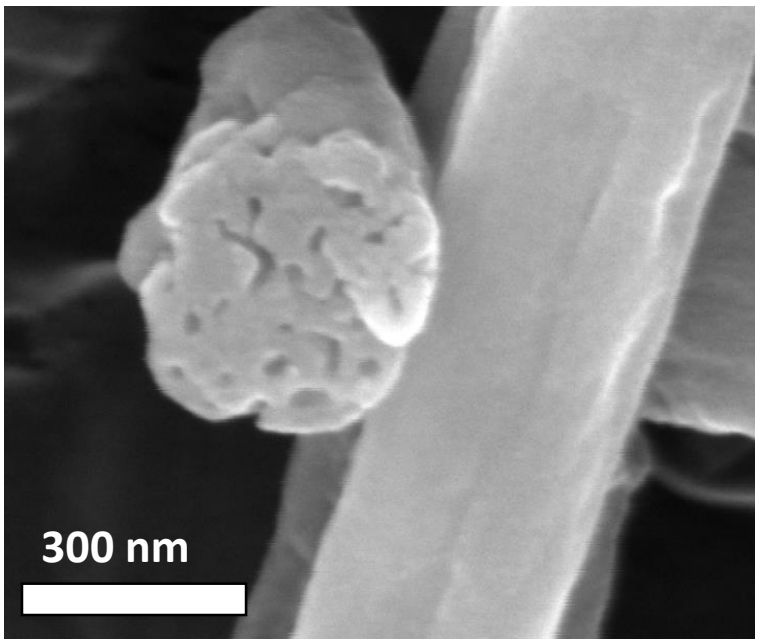


**Fig. S4.** SEM image of PAN:PMMA (80:20)

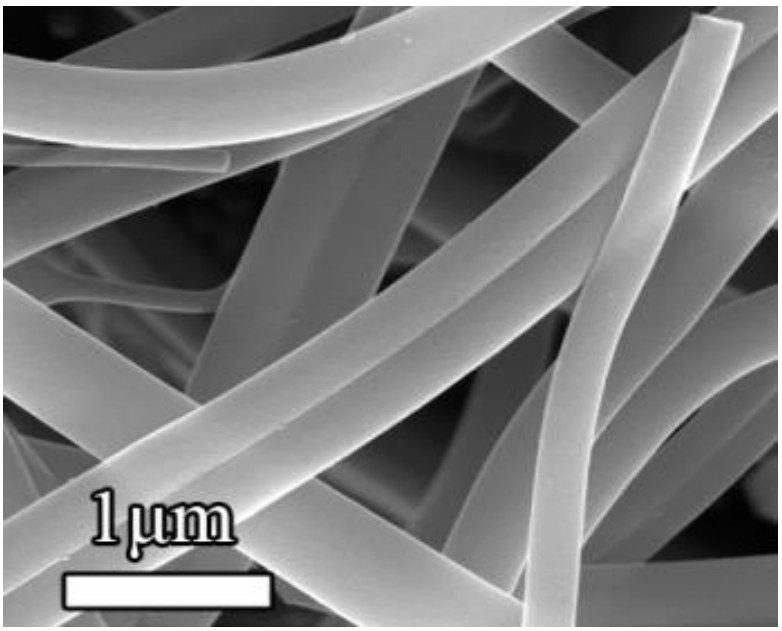


**Fig. S5.** SEM image of CNF.

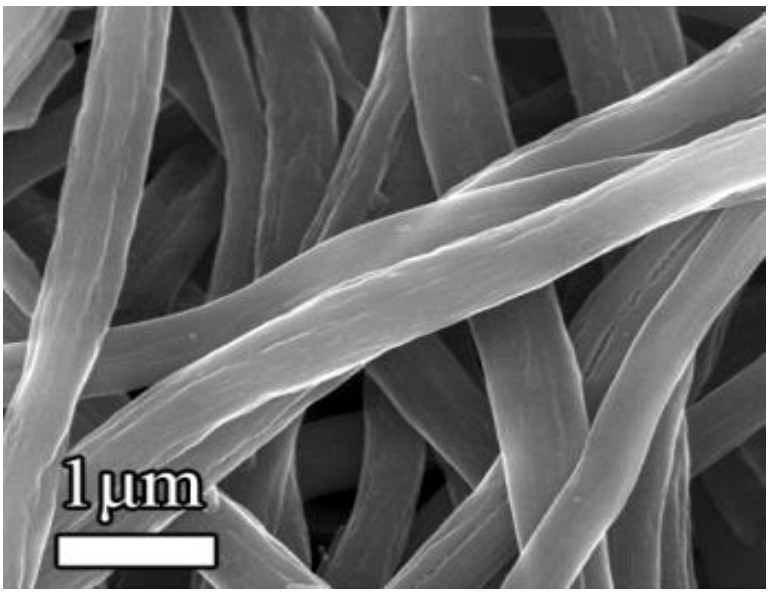


**Fig. S6.** SEM image of PCNF.

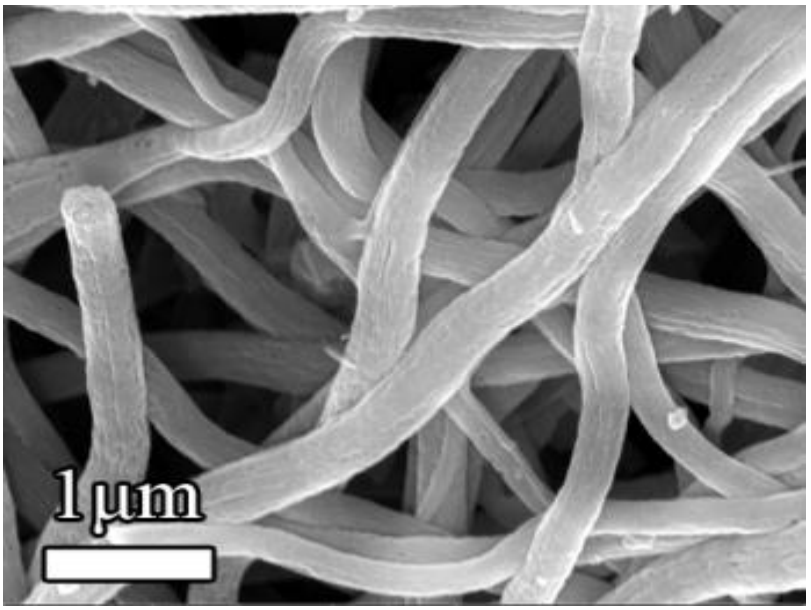


**Fig. S7.** SEM image of A-PCNF.

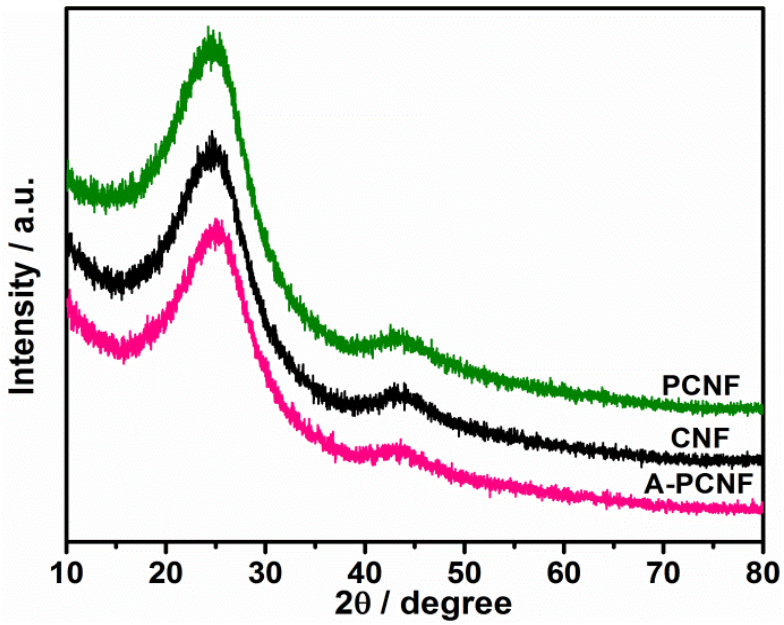


**Fig. S8.** XRD patterns of CNF, PCNF, and A-PCNF.

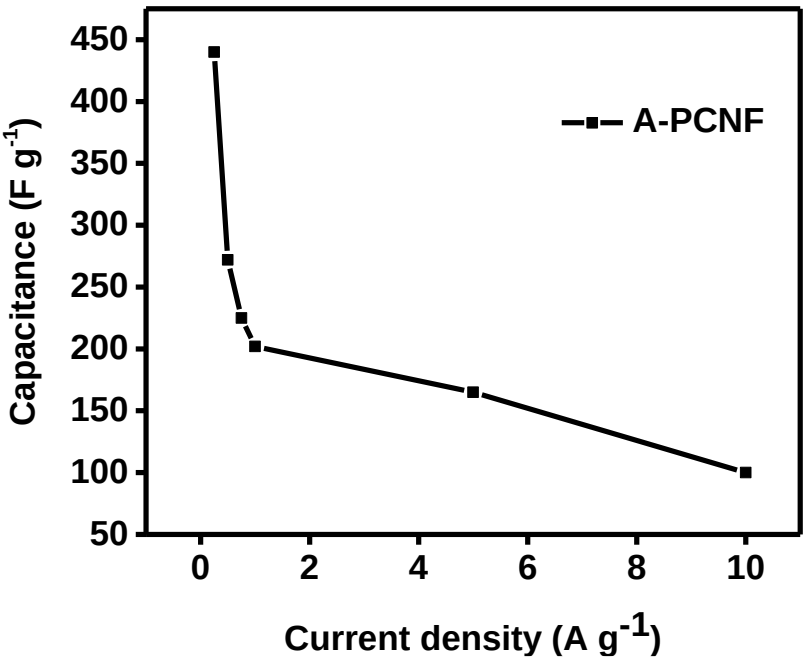


**Fig. S9.** Specific capacitances of A-PCNF at different current densities from 0.25 to 10 A $g^{-1}$.

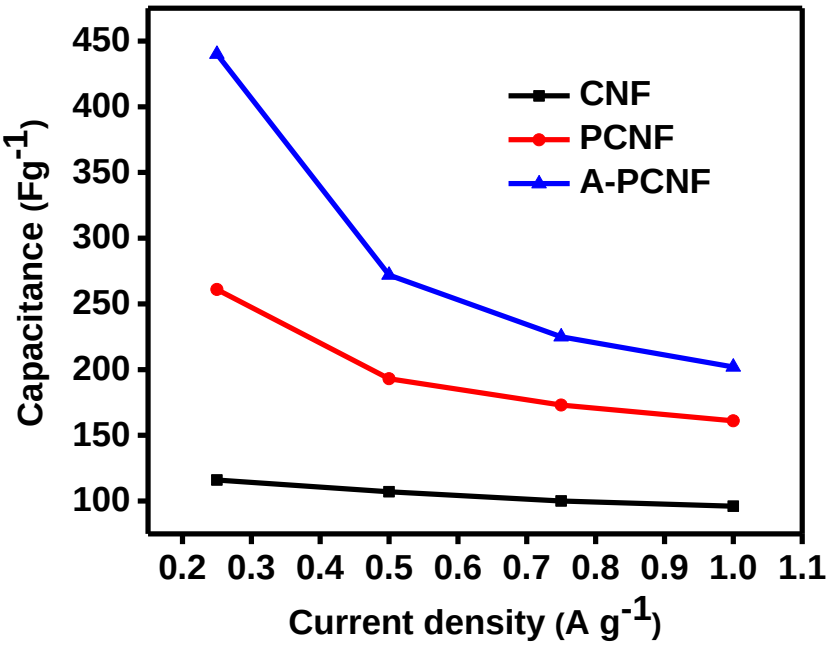


**Fig. S10.** Specific capacitances of CNF, PCNF, and A-PCNF at different current densities from 0.25 to 1 A $g^{-1}$

## References


1. G. Yu, X. Xie, L. Pan, Z. Bao, Y. Cui, *Nano Energy*, 2 (2013) 213.
2. X. Chen, B. Zhao, Y. Cai, M.O. Tade, Z. Shao, *Nanoscale*, 5 (2013) 12589.
3. S. Roldan, D. Barreda, M. Granda, R. Menendez, R. Santamaria, C. Blanco, *Phys. Chem. Chem. Phys.*, 17 (2015) 1084.
4. P. He, L. Liu, W. Song, G. Xiong, T.S. Fisher, T. Chen, *RSC Adv.*, 5 (2015) 31837.
5. Y. Huang, J. Liang, Y. Chen, Small, 8 (2012) 1805.
6. J. Shen, C. Yang, X. Li, G. Wang, *ACS Appl. Mater. Interfaces*, 5 (2013) 8467.
7. M. Sevilla, L. Yu, L. Zhao, C.O. Ania, M.-M. Titiricic, *ACS Sustainable Chem. Eng.*, 2 (2014) 1049.
8. M. Inagaki, Y. Yang, F. Kang, *Adv. Mater.*, 24 (2012) 2547.
9. Y. Meng, K. Wang, Y. Zhang, Z. Wei, *Adv. Mater.*, 25 (2013) 6985.
10. X. Xiao, X. Peng, H. Jin, T. Li, C. Zhang, B. Gao, B. Hu, K. Huo, J. Zhou, *Adv. Mater.*, 25 (2013) 5091.
11. S. Giri, D. Ghosh, C.K. Das, *Adv. Energy Mater.*, 24 (2014) 1312.
12. K. Wang, L. Li, T. Zhang, Z. Liu, *Energy*, 70 (2014) 612.
13. J. Chmiola, C. Largeot, P.L. Taberna, P. Simon, Y. Gogotsi, *Science*, 328 (2010) 480.
14. L.L. Zhang, X.S. Zhao, *Chem. Soc. Rev.*, 38 (2009) 2520.
15. Y. Cheng, L. Huang, X. Xiao, B. Yao, L. Yuan, T. Li, Z. Hu, B. Wang, J. Wan, J. Zhou, *Nano Energy*, 15 (2015) 66.
16. X. Lu, C. Shen, Z. Zhang, E. Barrios, L. Zhai, *ACS Appl. Mater. Interfaces*, 10 (2018) 4041.
17. R. Pai, A. Singh, S. Simotwo, V. Kalra, *Adv. Energy Mater.*, 20 (2018) 1701116.
18. J. Cai, H. Niu, Z. Li, Y. Du, P. Cizek, Z. Xie, H. Xiong, T. Lin, *ACS Appl. Mater. Interfaces*, 7 (2015) 14946.

19. D. Xu, Q. Xu, K. Wang, J. Chen, Z. Chen, *Acs Appl. Mater. Interfaces*, 6 (2014) 200.
20. A. Greiner, J.H. Wendorff, *Angew. Chem., Int. Ed.*, 46 (2007) 5670.
21. J. Zheng, K. Liu, D.H. Reneker, M.L. Becker, *J. Am. Chem. Soc*., 134 (2012) 17274.
22. H. An, H.-J. Ahn, *Mater. Lett.*, 93 (2013) 88.
23. Y.-E. Miao, J. Yan, Y. Huang, W. Fan, T. Liu, *RSC Adv.*, 5 (2015) 26189.
24. B.-H. Kim, C.H. Kim, D.G. Lee, *J. Electroanal. Chem.*, 760 (2016) 64.
25. D.-Y. Lee, G.-H. An, H.-J. Ahn, *J. Ind. Eng. Chem.*, 52 (2017) 121.
26. G.Z. Lei Wang, Xiaojia Zhang, Huimin Shi, Wei Zeng, Hang Zhang, Qing Liu, Chengchao Li, Quanhui Liua and Huigao Duan, *J. Mater. Chem. A*, 5 (2017) 14801.
27. Y. Wang, J. Yang, R. Du, L. Chen, *ACS Appl. Mater. Interfaces*, 9 (2017) 23731.
28. C. Kim, B.T.N. Ngoc, K.S. Yang, M. Kojima, Y.A. Kim, Y.J. Kim, M. Endo, S.C. Yang, *Adv. Mater.*, 19 (2007) 2341.
29. L. Fan, L. Yang, X. Ni, J. Han, R. Guo, C. Zhang, *Carbon*, 107 (2016) 629.
30. J.H. Yingbo Xiao, Yazhou Xu, Hui Zhu, Kai Yuan , a.Y. Chen, *J. Mater. Chem. A*, 6 (2018) 9161.
31. S.-C. Lin, Y.-T. Lu, Y.-A. Chien, J.-A. Wang, P.-Y. Chen, C.-C.M. Ma, C.-C. Hu, *J. Power Sources*, 393 (2018) 1.
32. N.C. Abeykoon, J.S. Bonso, J.P. Ferraris, *RSC Adv.*, 5 (2015) 19865.
33. S. Shilpa, A. Sharma, *RSC Adv.*, 6 (2016) 78528.
34. S. Zheng, H. Ju, X. Lu, *Adv. Energy Mater.*, 5 (2015) 1500871.
35. C. Ma, X. Chen, D. Long, J. Wang, W. Qiao, L. Ling, *Carbon*, 118 (2017) 699.
36. Y. Zhang, S.-J. Park, *Carbon*, 122 (2017) 287.
37. X. Tian, H. Ma, Z. Li, S. Yan, L. Ma, F. Yu, G. Wang, X. Guo, Y. Ma, C. Wong, *J. Power Sources*, 359 (2017) 88.
38. D.W. Lawrence, C. Tran, A.T. Mallajoysula, S.K. Doorn, A. Mohite, G. Gupta, V. Kalra, *J. Mater. Chem. A*, 4 (2016) 160.
39. G.-H. An, B.-R. Koo, H.-J. Ahn, *Phys. Chem. Chem. Phys.*, 18 (2016) 6587.
40. D.G. Lee, J.H. Kim, B.-H. Kim, *Electrochim. Acta*, 200 (2016) 174.
41. C.H. Kim, B.-H. Kim, *Electrochim. Acta*, 117 (2014) 26.
42. X. Ning, W. Zhong, S. Li, Y. Wang, W. Yang, *J. Mater. Chem. A*, 2 (2014) 8859.
43. W. Zhou, K. Zhou, X. Liu, R. Hu, H. Liu, S. Chen, *J. Mater. Chem. A*, 2 (2014) 7250.
44. Z.-Y. Yu, L.-F. Chen, L.-T. Song, Y.-W. Zhu, H.-X. Ji, S.-H. Yu, *Nano Energy*, 15 (2015) 235.
45. Y. Liu, J. Zhou, L. Chen, P. Zhang, W. Fu, H. Zhao, Y. Ma, X. Pan, Z. Zhang, W. Han, E. Xie, *ACS Appl. Mater. Interfaces*, 7 (2015) 23515.
46. Y. Liu, G. Jiang, S. Sun, B. Xu, J. Zhou, Y. Zhang, J. Yao, *J. Electroanal. Chem.*, 804 (2017) 212.
47. W.J. Youe, S.J. Kim, S.M. Lee, S.J. Chun, J. Kang, Y.S. Kim, *Int. J. Biol. Macromol*., 112 (2018) 943.
48. N. Cai, J. Fu, H. Zeng, X. Luo, C. Han, F. Yu, *J. Alloys Compd.*, 742 (2018) 769.
49. X. Wang, C. Lu, H. Peng, X. Zhang, Z. Wang, G. Wang, *J. Power Sources*, 324 (2016) 188.